

Survival of *P. falciparum* infected Red Blood Cell Aggregates in Elongational Shear Flow

Anna Joetten

University of Augsburg

Anabelle Schepp

University of Augsburg

Adam Machon

University of Edinburgh

Kirsten Moll

Karolinska Institute

Mats Wahlgren

Karolinska Institute

Timm Krueger

University of Edinburgh

Christoph Westerhausen (✉ christoph.westerhausen@gmail.com)

University of Augsburg

Research Article

Keywords: Malaria, microfluidics, red blood cells, aggregation, stability, shear flow, FEM, two state model

Posted Date: April 4th, 2022

DOI: <https://doi.org/10.21203/rs.3.rs-1521580/v1>

License:  This work is licensed under a Creative Commons Attribution 4.0 International License.

[Read Full License](#)

Survival of *P. falciparum* infected Red Blood Cell Aggregates in Elongational Shear Flow

Anna Jötten¹, Anabelle Schepp¹, Adam Machon², Kirsten Moll³, Mats Wahlgren³, Timm Krüger², Christoph Westerhausen^{1,4,5,*}

¹Institute of Physics, University of Augsburg, 86159 Augsburg, Germany

²School of Engineering, Institute for Multiscale Thermofluids, University of Edinburgh, Edinburgh EH9 3FB, UK

³Department of Microbiology, Tumor and Cell Biology, Karolinska Institutet, 171 77 Stockholm, Sweden

⁴Center for NanoScience (CeNS), Ludwig-Maximilians-Universität, Munich 80799, Germany

⁵Institute of Theoretical Medicine, University of Augsburg, 86159 Augsburg, Germany

*author to whom correspondence should be addressed: christoph.westerhausen@gmail.com

ABSTRACT

Rosetting, the formation of red blood cell aggregates, is a life-threatening condition in *Malaria tropica* and not yet fully understood. We study rosette stability using a set of microfluidic stenotic channels, with varied narrowing angle and erythrocytes of blood groups O and A. We find reduced ability of a rosette to pass a stenosis without disruption, the longer the tapered part of the constriction and the narrower the stenosis is. In general, this ability increases with rosette size and is 5%-15% higher in blood group A. The experimental results are substantiated by equivalent experiments using lectin-induced red blood cell aggregates, a simulation of the underlying protein binding kinetics, and lattice-Boltzmann-finite-element simulations of red blood cell aggregates.

SIGNIFICANCE STATEMENT

The WHO reported an estimated number of 241 million cases and 627 000 malaria deaths in 2020. The most lethal form is *Malaria tropica* due to erythrocyte aggregates blocking blood flow in capillaries, especially in the brain. It has been shown that the stability of these aggregates under flow is size and blood group dependent. However, it is unclear which physical interaction determines the aggregates fates during passing constrictions. We here show that for different elongational and shear flow application the exposition duration of elongational flow is more relevant than its absolute value, explaining why the aggregates survive the passage of stenoses with an abrupt reduction of the vessel cross section more easily than those with a lower elongational rate.

INTRODUCTION

The malaria parasite invades red blood cells and causes them to coagulate and form so-called *rosettes*. Rosette formation covers the binding proteins, which are expressed during parasite development, with healthy red blood cells. Consequently, rosetting avoids attacks from the immune system (1, 2). Rosettes can lead to emboli causing arterial blockage, which results in insufficient supply of oxygen to the tissue (3). Blood clots or arterial embolisms that are promoted by rosetting can be fatal for people who suffer from heart diseases (4, 5).

The stability of rosettes has been studied since the 1990s, but the binding mechanisms are not fully uncovered (6). Nash et al. used cone-and-plate viscometers (7, 8) and micropipettes (7) to unravel that rosettes can form and persist under physiological wall shear stress, which ranges from 0.05 Pa in post-capillary venules to 1 Pa in arteries (8). Wall shear stress of 1 Pa corresponds to a force of 10^{-10} N on two cohesive cells (8). Using a viscometer to apply shear stress, rosettes withstand this stress for minutes, while applying the same force using a micropipette disrupts the rosette in seconds (8). Adams et al. studied rosetting in microfluidic flow assays (diameter 800 μm) and found no effect of shear stress between 0.05 Pa and 0.1 Pa (9). These studies, however, did not take the physical confinement in capillaries into account.

To address the open question of rosette stability under different flow conditions, in a previous publication we quantified rosette survival using a set of stenotic channels of different widths of constrictions between 3.5 μm and 14.5 μm (10). We found a correlation of rosette size, channel diameter and blood group regarding the rosettes' stability or ability to deform. Our data revealed that, under physiologically relevant conditions, rosettes in blood group A have a higher frequency and stability compared to blood group O, contributing to the explanation of the mechanism underlying the observed protection against severe malaria in non-O individuals (10).

We know from other (binding) proteins such as von-Willebrand-Factor (vWF), a key player in blood clotting, that mainly the elongational components of flow drive the activation of vWF (11). The different effects of shear and elongational flow is due to the fact that shear flow contains a rotational component that leads to tumbling instead of stretching (11). However, it is still unclear if in case of rosettes the elongational rate has a similar predominant impact compared to simple shear flow as on vWF. As a working hypothesis, we here assume that this is indeed the case.

Following our hypothesis, we refined the set of stenoses, keeping the constriction width close to the above-mentioned critical width, and varying the elongational length or the steepness of the narrowing part of the stenosis. This approach allows us to separate the influence of the shear rate perpendicular to the flow and the elongation rate along the direction of the flow. We continue studying rosetting in blood groups O and A and classifying the rosettes by size. Additionally, we use lectin-induced red blood cell aggregates as a model system and perform the same experiments on those. A simulation of the underlying protein binding kinetics, based on Kramers' theory and a simple Monte Carlo simulation of a two-state-model (bound and unbound state) complements the experimental results. We complete the study with three dimensional lattice-Boltzmann-finite-element simulations of red blood cell aggregates, comprised of one parasitized cell and several unparasitized ones, which deform and potentially detach passing a stenosis imitating the experiment.

METHODS

Sample Preparation

We cultivated the *P. falciparum* laboratory strain S1.2 (12) according to standard methods and synchronized it using 5% sorbitol (12). Prior to experiments, we identified the stage of the parasite by staining of fresh culture with Acridine Orange and subsequent microscope analysis. We enriched the parasitized red blood cells (pRBCs) around 32–38 hr *post invasion* by magnetically activated cell sorting (MACS, Miltenyi Biotec), as described earlier (12), resulting in 70–90% parasitemia. We resuspended the enriched pRBCs with unparasitized RBCs in MCMS, malaria culture medium containing 10% filtered human serum, to reach a final parasitemia of 20% and a hematocrit of 1%. The added unparasitized RBCs were of blood group O and A for the measurements in the respective blood groups, while blood group O RBCs were used for cultivation of the parasite. After two hours of incubation, rosettes have formed. A rosette is by definition composed of one infected and at least two unparasitized cells. Other forms of aggregation like auto-agglutination between infected cells and rosettes with more than one infected cell can occur, but these aggregates form rarely, as reviewed by optical controls.

Microchannel Design and Measurement Setup

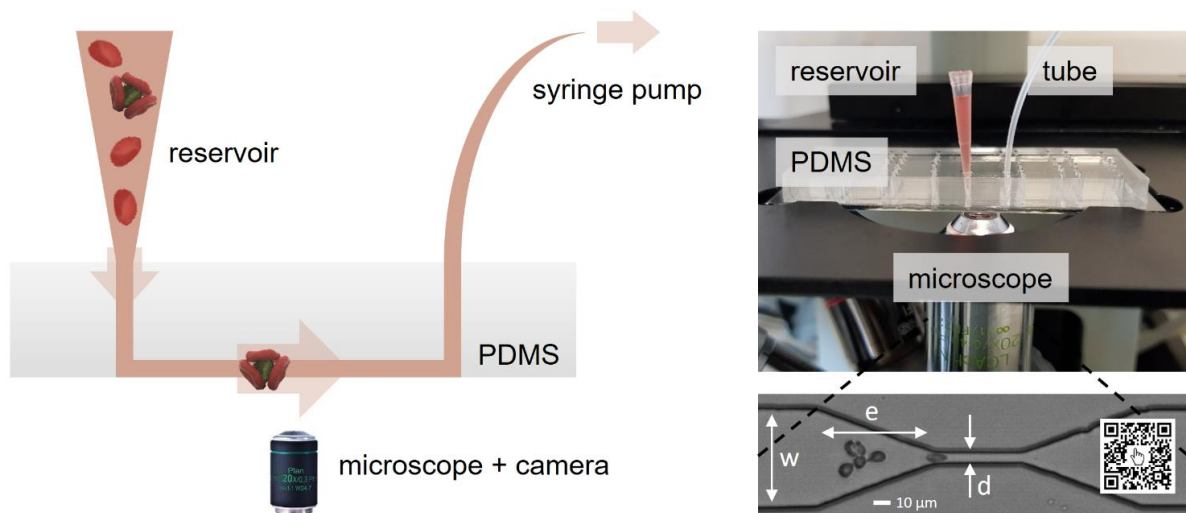


Figure 1 Microfluidic setup consisting of a microfluidic channel in PDMS on a glass slide, a pipette tip as sample reservoir at the channel inlet and a PTFE tube at the channel outlet connected to a syringe pump. The channel width w is gradually reduced to the stenosis diameter d over the length e . Micrographs are recorded using an inverted microscope.

The microchannel consisted of a polydimethylsiloxane (PDMS) single layer fabricated by standard soft lithography (13), which was bonded on a glass slide by plasma activation (Fig. 1). Generally, all channels in our set were 7 mm long, 8 μm in depth and 50 μm in width. The central part of interest comprised a single stenosis in which the channel width was reduced from $w = 50 \mu\text{m}$ to one of the two chosen values $d = 5 \mu\text{m}$ and $d = 7 \mu\text{m}$, respectively, if not mentioned otherwise. Four differently steep stenoses were combined with each constriction width (Figure 2). The length of the stenosis designated as “standard elongation” complies with a narrowing angle of 20° or an elongational length e of $e = e_{std} = 55 \mu\text{m}$. One steeper angle, resulting in “one fifth elongation”, $e = 0.2e_{std}$, and two smaller angles complying with “double elongation” ($e = 2e_{std}$) and “triple elongation” ($e = 3e_{std}$) were chosen.

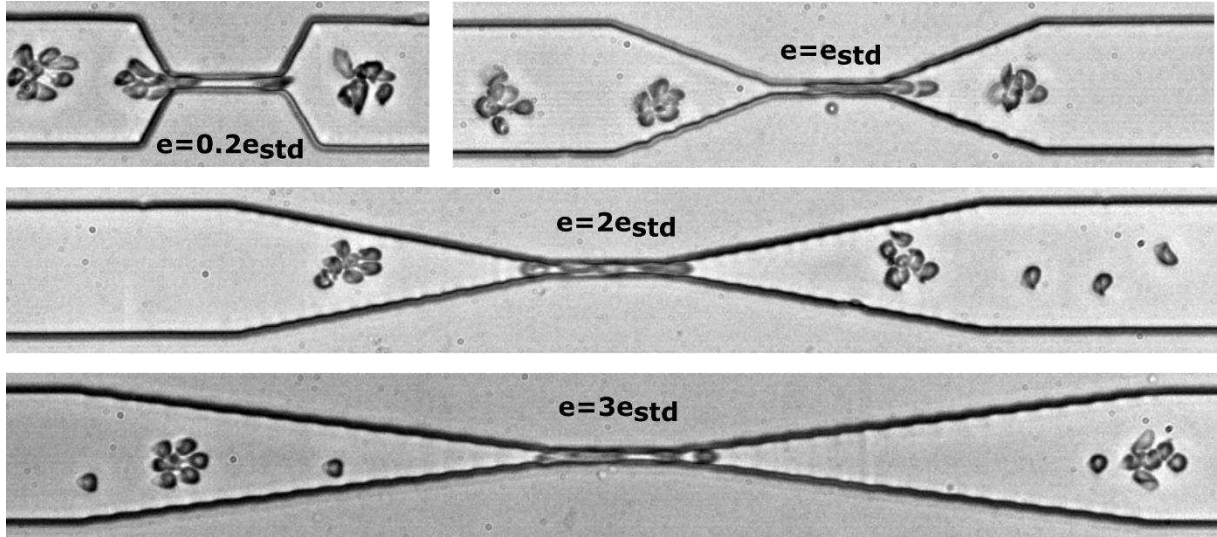


Figure 2 Set of different stenoses used in the experiments. All channels are constantly $8 \mu\text{m}$ deep and initially $50 \mu\text{m}$ wide, narrowing to a stenosis of $5 \mu\text{m}$ width (or $7 \mu\text{m}$, not shown) over a varied elongational length of $e = 0.2e_{std}$; e_{std} ; $2e_{std}$ and $3e_{std}$ with $e_{std} = 55 \mu\text{m}$.

The complete setup as depicted in Figure 1 consisted of the microchannel, a pipette tip serving as the cell suspension reservoir and a syringe pump (Harvard PHD2000, Harvard Apparatus). A Hamilton Gastight Syringe (Hamilton Bonaduz AG) containing phosphate-buffered saline (PBS, pH = 7.4) was connected to the microchannel via a polyfluoroethylene (PTFE) tube (inner diameter 0.38 mm). The pump was operated in reverse mode to provide controlled flow by drawing the suspension from the reservoir through the microfluidic channel. We observed the cells using the 20x objective of an inverted microscope (Nikon Diaphot 300) equipped with a high speed video camera (FASTCAM Mini UX50 type 160K-M-16G, Photron). The videos were recorded with the software Photron Fastcam Viewer PFV from Photron at 2000 frames per second, 1280×120 pixel resolution, and $1/32000$ seconds exposure, resulting in a maximum total of 74531 frames or 37 seconds in real time covering an area of $704 \times 66 \mu\text{m}^2$.

SURF tracing and categorizing

For analysis we developed the customized software SURF (SUrvival of Rosettes in Flow), a MATLAB© based tracking algorithm to follow and analyze rosettes along a microfluidic channel. The functionality was published earlier (10, 14).

Categorize by size. The “size” of the rosettes A_{ros} denotes here the cross-sectional area as optically appearing in the micrographs. The rosettes’ radius r_{ros}

$$r_{ros} = \sqrt{A_{ros}/\pi} \quad (1)$$

is the radius of the equivalent circle with area A_{ros} , respectively. For further analysis, these traces are categorized according to the initial rosette size A_{ros} being normalized to the area of a single red blood cell A_{RBC} . The histogram edges used are set to 1.11, 2.22, 3.33, 4.44, 5.56, 7.78 and $30 A_{RBC}$, and classified into classes 1–6. Cell aggregates in class 1 consist often only of two cells. A rosette is by definition composed of one infected and at least two unparasitized cells, therefore only cell aggregates from classes 2–6 are taken into account in the results section.

Categorize by fate. If a rosette is being traced along the channel, main events such as rupture and total disruption are identified and listed (compare (10)). Following a rosette squeezing

through a stenosis, one of three possible scenarios can be observed: (i) a rosette can either pass undamaged, or (ii) damaged, i.e., suffering from a certain cell loss but still being large enough to be considered a rosette, or (iii) become totally disrupted, i.e. losing so many cells that the remaining aggregate falls into class 1.

Simulation of the protein binding kinetics

Since cell adhesion is mediated by proteins (15, 16), a theoretical model of such proteins is developed and described here. This is based on the principle that a protein can either be in the state "bound" (1) or "detached" (0), and within a time period Δt with a probability P , which is the product of the binding or unbinding rate k and the time span Δt . Thus, for a single protein, a simple random experiment can be performed by creating a (pseudo) random number $z \in [0, 1)$ that is compared with the probability P . If one simulates the behavior of several such proteins in parallel, the model can be applied to the disintegration or cohesion of entire cell aggregates. In concrete terms, the simulation is implemented as follows: First, the intrinsic tie-off and tie-on rates $k_{on,0}$ and $k_{off,0}$ are determined. The initial equilibrium constant K

$$K = \frac{k_{on,0}}{k_{on,0} + k_{off,0}} \quad (2)$$

determines how many of the N_{total} proteins are in the bound state at the beginning. This means

$$N_{on,0} = KN_{total}. \quad (3)$$

In the example in Figure 7, at the beginning, $N_{on,0} = 5$ proteins of the $N_{total} = 10$ proteins are in the bound state "1", the remaining $N_{total} - N_{on,0} = 5$ in the unbound state "0". In each simulation step, a random experiment now takes place for each protein. For this purpose, the rates k_{on} and k_{off} must be known. In general, the rate according to Kramers (16–18) depends on the force F acting on the protein and the distance between initial and transition state x ,

$$k_{off} = k_{off,0} e^{\frac{Fx}{k_B T}}. \quad (4)$$

The force F acting here is mainly the drag force, which is a function of the square of the velocity. Thus, to reproduce the experiment of the passage of a stenosis, the velocity $v(t)$ must be included into the calculation of the rate. The force per protein can be estimated by the number of proteins on the surface of an infected red blood cell. The surface has approximately 1000 knobs, each of which has approximately 100 proteins expressed on it (19); this results in $N_{proteins} \approx 100.000$. The ratio $\frac{F}{N_{proteins}}$ is given by the product of a constant c' and the square of the velocity.

$$\frac{F}{N_{proteins}} = c'v^2 \quad (5)$$

Moreover, assuming a constant distance x , meaning protein stretching, between the initial state and the transition state we summarize c' and the constant $x/k_B T$ in the constant c .

$$\begin{aligned} k_{on} &= k_{on,0} e^{-cv^2} \\ k_{off} &= k_{off,0} e^{cv^2} \end{aligned} \quad (6)$$

Furthermore, the force is distributed exclusively among the bound proteins. Thus, the force must be corrected by the factor $\frac{N_{total}}{N_{on}}$.

$$\begin{aligned} k_{on} &= k_{on,0} e^{-\frac{N_{total} c v^2}{N_{on}}} \\ k_{off} &= k_{off,0} e^{\frac{N_{total} c v^2}{N_{on}}} \end{aligned} \quad (7)$$

The initial conditions are set by the fixed, but arbitrarily chosen, parameters $k_{on,0} = 1000$ and $k_{off,0} = 200$. The value of the parameter c is estimated from the drag force as follows:

$$c v^2 = \frac{F x}{N_{proteins} k_B T} = \frac{\frac{1}{2} \rho C_W r^2 \pi v^2 x}{N_{proteins} k_B T} \approx 130 v^2 \quad (8)$$

The drag force is expressed by the fluid density $\rho = 1000 \frac{kg}{m^3}$, the drag coefficient $C_W = \frac{24}{r}$, the rosette radius r and the flow velocity v . A rosette radius of $r = 12 \mu m$ is chosen here to calculate c . For other rosette sizes correspondingly different values between $c = 90$ for $r = 10 \mu m$ and $c = 200$ for $r = 15 \mu m$. In addition, the value depends on the choice of the characteristic bond length $x = 1$ nm and the Reynolds number, which is kept constant here at $Re = 0.1$. To reproduce the velocity course of a stenosis, in each time step Δt the travelled distance Δx is calculated from the current velocity. Then, at the new position the new velocity is calculated over the current channel width d as a function of elongation length e and length of the narrowest part of the stenosis l .

If at least one of the simulated N_{total} "proteins" or binding sites is still bound after passage of the location of the stenosis in the simulation, it has "survived", and the equilibrium $N_{on,0}$, which prevailed before the stenosis, can be restored. If, at any time, all proteins are detached simultaneously, the aggregate is considered disintegrated, and rebinding is no longer possible. Such an aggregate has "not survived." For multiple runs r of the simulation with a group of N_{total} proteins, it is possible to determine a survival rate s_{sim} based on the number of runs in which the stenosis was survived $r(N_{on,end} > 1)$, and the total number of runs r_{total} .

$$s_{sim} = \frac{r(N_{on,end} > 1)}{r_{total}} \quad (9)$$

Lattice-Boltzmann-finite-element simulations

A standard single-relaxation time lattice-Boltzmann method on a D3Q19 lattice is used to solve the Navier-Stokes equations governing the fluid flow (20). Red blood cells are modelled as deformable biconcave capsule membranes with in-plane shear, area dilation and bending elasticities. The red blood cell membranes are discretized by a set of flat triangular elements, and a finite-element method is used to calculate the membrane forces of the red blood cells in their deformed state (21). The immersed boundary method with a 2-point stencil couples the fluid and membrane dynamics (22), and the half-way bounce-back method is used to impose the no-slip condition at the surface of the microfluidic geometry (23). Periodic

boundary conditions are used along the flow axis. A body force is used to drive the flow, mimicking a pressure drop along the channel.

In order to simulate the aggregate, we consider a single infected and a varying number of uninfected RBCs. The Morse interaction potential between pairs of neighboring RBC surface nodes used:

$$V = S[\exp(2\beta(r_0 - r)) - 2\exp(\beta(r_0 - r))], \quad (10)$$

where S is the interaction strength, β is a shape parameter, r_0 is the equilibrium distance, and r is the distance between two neighboring RBC surface nodes. The interaction potential is only active when the infected and an uninfected RBC interact; pairs of uninfected RBCs do not interact through the Morse potential.

RESULTS AND DISCUSSION

State of the Rosettes after passing a stenosis

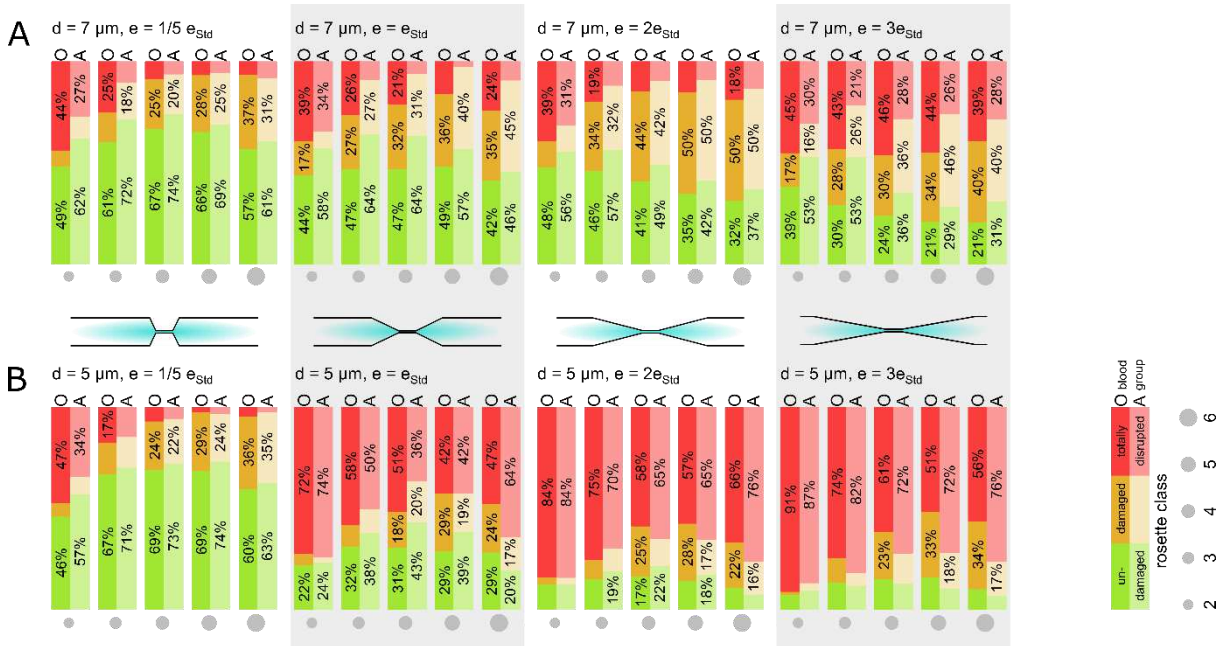


Figure 3 The state of a rosette after passing a stenosis is either „undamaged“ (green), „damaged“ (yellow) or „totally disrupted“ (red). The bar charts show the distribution on those three states for stenoses of two different widths A) $d = 7 \mu\text{m}$, B) $d = 5 \mu\text{m}$ and four different elongational lengths. Besides the standard elongation measuring $e_{Std} = 55 \mu\text{m}$, there is one shorter version with $e = 0.2e_{Std}$ and two longer versions with $e = 2e_{Std}$ and $e = 3e_{Std}$. The area of the grey circles represents the size of a rosette of the respective rosette class (10). Results in blood groups A and O are labelled A and O, respectively.

The colored bars in Figure 3 A and B depict the distribution of rosette states for blood group O and A directly after passing a stenosis of width $7 \mu\text{m}$ and $5 \mu\text{m}$, respectively. From left to right, the elongation length is varied from $0.2 e_{Std}$ to $3 e_{Std}$. These states are denoted (i) undamaged (green), (ii) damaged (orange) and (iii) totally disrupted (red). Both figures summarize the results of 500–1500 traced rosettes being classified into categories 2–6. The experiments result in 95% confidence intervals of 5% on average.

We confirm two effects that we have reported earlier (10). Firstly, the percentage of totally disrupted rosettes is higher for smaller rosettes than for larger ones. Secondly, more rosettes are disrupted passing the narrower stenosis with $d = 5 \mu\text{m}$ than the one with $d = 7 \mu\text{m}$. Beyond these observations, we found a significant impact of the elongational length that has not been investigated previously. The longer the stenosis, the fewer rosettes pass without damage. Comparing the survival rate, which comprises the undamaged and damaged rates (green and orange bars), between both diameters $d = 5 \mu\text{m}$ and $d = 7 \mu\text{m}$ at each elongational length individually, we find almost equal results for the shortest stenosis ($e = 0.2e_{Std}$), while longer stenoses lead to significantly lower survival rates for the $d = 5 \mu\text{m}$ stenosis. The impact of the length of the stenosis is remarkably smaller for the wider stenosis with $d = 7 \mu\text{m}$: for all values of e , the survival rate ranges from 75% to 90%. For the narrower stenosis with $d = 5 \mu\text{m}$, however, the results cover a much wider range from 30% to 85%. The longer the stenosis, the fewer rosettes remain undamaged. An abrupt constriction, accompanied with a higher elongation rate, seems to affect a rosette less than the continuous extension when passing a longer stenosis. This is in contradiction to our initial working hypothesis. The leading cause,

besides the immediate lengthening of the rosette, could be the longer exposure time to higher shear and elongational stresses in longer stenoses.

When comparing rosettes with different sizes (between class 3 and 6), we find a decreasing percentage of undamaged rosettes. At the same time, the percentage of damaged rosettes increases to such an extent that the total survival rate slightly increases with rosette size. Comparing blood groups O and A, the survival rate is 5-15% higher in blood group A. Both the size and blood group effects are in line with earlier works (10). Exceptions occurred at $d = 5 \mu\text{m}$ with $e = 2e_{std}$ and $e = 3e_{std}$, where the survival rate of blood group O rosettes exceeds those of blood group A.

Transition Length

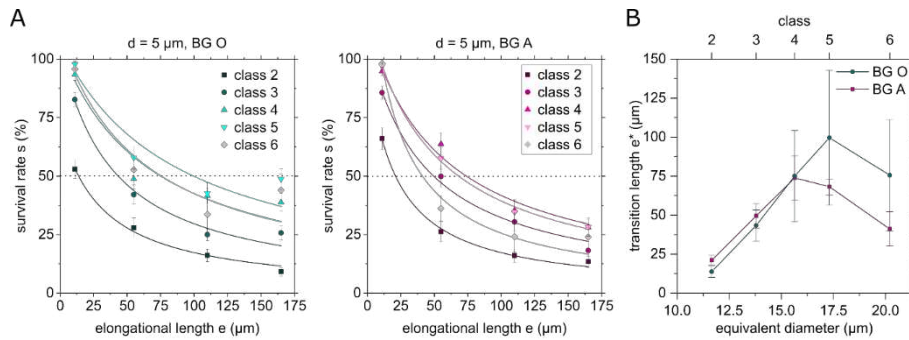


Figure 4 Impact of the elongation in a stenosis on the disruption of rosettes. A) Survival rate of rosettes of rosette classes 2–6 in blood group O (left) and A (right) as a function of elongational length when passing stenoses of different lengths and fixed width of $d = 5 \mu\text{m}$ fitted using equation 11. Error bars are 95% confidence intervals. B) Transition length e^* , which results from fits in A, as a function of the rosette size. The transition length e^* is defined as the critical length beyond which the survival rate drops below 50%.

Plotting the survival rate as a function of the elongational length e , reveals a hyperbolic relation. The phenomenological fit function $s(c, e)$ describes the survival rate s for rosette class c as a function of the elongational length e using the descriptive parameters p and q :

$$s(c, e) = \frac{1}{p + qe} \quad (11)$$

From the fit function, the length e^* that corresponds to a survival rate of 50% can be calculated:

$$s(c, e) = 0.5 \quad (12)$$

The curves in Figure 4 correlate with values of $p \approx 1$ and $q \approx 0.02 \mu\text{m}^{-1}$. Accordingly, the transition length falls with $e^* \approx 50 \mu\text{m}$ into the experimental range and increases with aggregate size, see Figure 4B. The difference between blood groups is not significant.

Looking at wider stenoses with $d = 7 \mu\text{m}$, the influence of the elongational length is negligible. As the respective curves never drop below $s = 50\%$, we do not explicitly show them or extract a transition length here.

Experimental Model: Lectin-induced aggregation

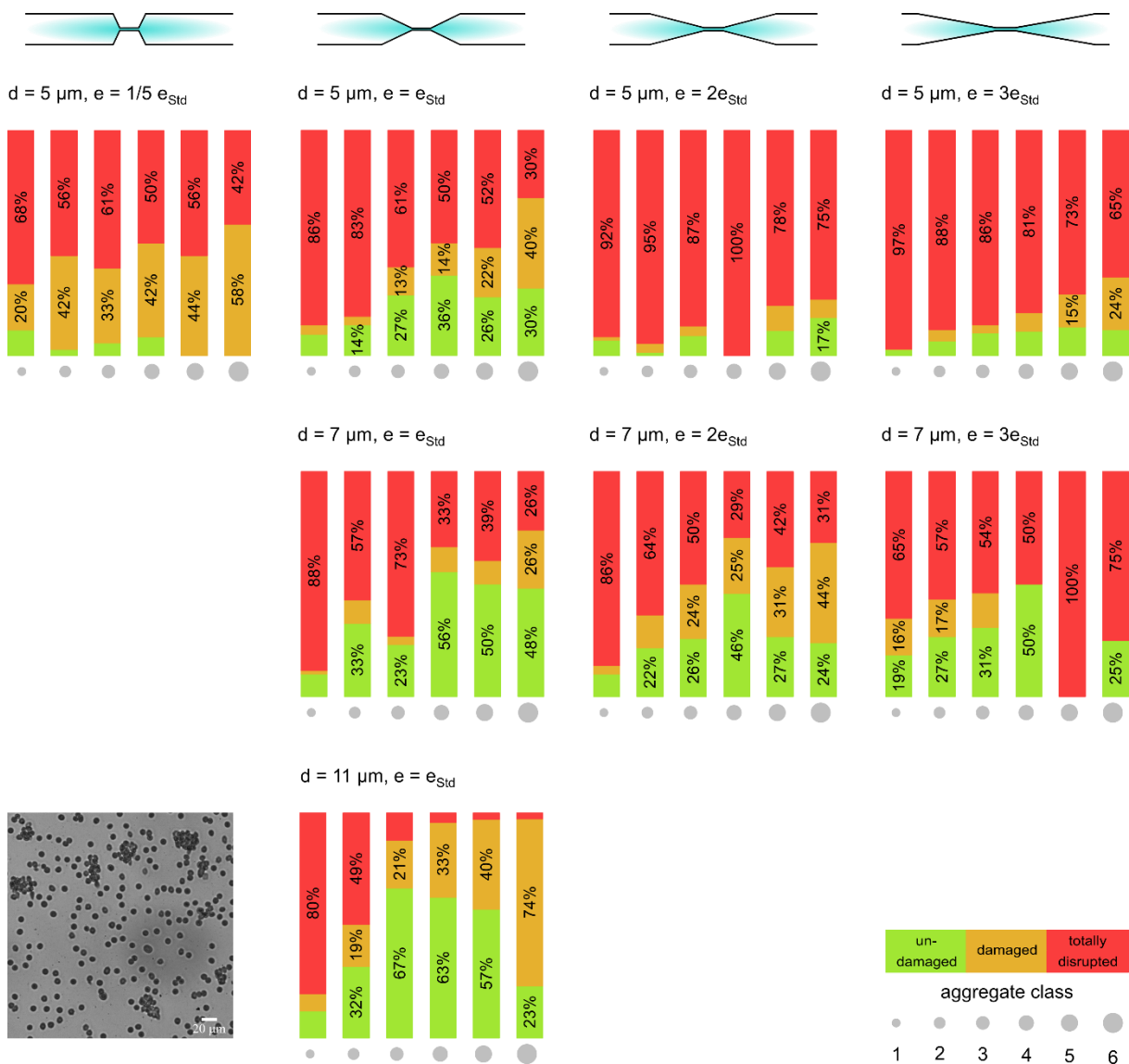


Figure 5 States of lectin-induced aggregates after passing different stenoses. The state of a lectin-induced aggregate after passage of a stenosis is either "undamaged" (green), "damaged" (yellow) or "totally disrupted" (red). The distribution among these three states for stenoses of three different widths ($d = 11 \mu\text{m}$, $d = 7 \mu\text{m}$, and $d = 5 \mu\text{m}$) and different elongational lengths ($e = 0.2e_{\text{Std}}$, e_{Std} , $2e_{\text{Std}}$ and $3e_{\text{Std}}$), standard elongation length $e_{\text{Std}} = 55 \mu\text{m}$, is shown. The area of the gray circles at the bottom corresponds in each case to the size of the aggregates in the relevant class 1–6. Inset: Lectin-induced aggregation of red blood cells.

To compare rosetting to other types of binding and to further evaluate the stability of rosettes, the same flow experiments are performed with lectin-induced aggregates as a model system. Lectins bind to membrane receptors of erythrocytes and induce clumping. In contrast to rosettes, where an infected cell forms the center from which adhesion molecules protrude, in lectin-induced aggregation all cells behave equally regarding cell-cell adhesion. However, the interactions resemble one another (24) and we optimized the lectin concentration and protocol to produce aggregates, which are convincingly similar to rosettes in shape and size distribution (see inset Figure 5). We do not focus on the effect of the blood group here, but all lectin experiments shown here were performed with blood group A. Classification by size follows the lines established for malaria rosettes. Since there is no reason to ignore class 1 in this case, all aggregates of classes 1–6 are considered here.

The influence of the elongation length can be seen in Figure 5 from left to right. If the elongation length is increased at a stenosis width of $d = 5 \mu\text{m}$, a strong decrease of the survival rates can be seen, see Figure 5 top row. At the steepest elongation of $e = 0.2e_{std}$, almost 70% of the small aggregates are completely disrupted, whereas only a fraction of about 10% passes the stenosis unharmed. If the aggregates increase in size, up to 50% survive the stenosis, but significantly more are damaged in the process, until there are no undamaged aggregates left in classes 5 and 6. Increasing the stenosis length, the trend continues for the larger aggregates to pass the stenosis in significantly greater numbers. About 15% of the aggregates survive the standard length in class 1 and already 70% in class 6, with about 10-35% of the aggregates remaining completely intact. If the elongation is increased to two or three times the standard length, more than 90% of the aggregates in class 1 are already disintegrated. This value decreases continuously with increasing aggregate size until, in class 6, 75% or 65% of the aggregates remain undamaged. The rate of undamaged aggregates is consistently similar at about 10%. Particularly with triple elongation, the proportion of damaged aggregates increases significantly from 5% to 25%.

A similar behavior can be seen for the channels with a stenosis width of $d = 7 \mu\text{m}$, see Figure 5 second row. For the standard elongation and two- and threefold lengths, the undamaged rate increases from about 10% to a local maximum at class 4 with about 50%. In the standard case $e = e_{std}$, this level remains largely unchanged, but in the longer stenosis it falls back to 25%. Also here, the rate of damaged aggregates increases noticeably with aggregate size. Other than at $d = 5 \mu\text{m}$, this is twice as pronounced for the twofold elongation as for the standard length. Only the triple elongation deviates from this trend, which is probably due to the sparse data available. In the first three classes, approx. 15% of 15-40 aggregates are damaged; for larger aggregates, the counts are only 2-4; consequently, the distribution is not statistically significant. For all other measurements, the trajectories of 50-500 aggregates are included per measuring point, i.e. per class and channel shape. In Figure 6 the corresponding 95% confidence intervals are plotted.

Next, we discuss Figure 5, second column, to focus on different widths ($d = 5 \mu\text{m}$, $d = 7 \mu\text{m}$ and $d = 11 \mu\text{m}$) at fixed elongation $e = e_{std}$ and flow rate Q in the range $7 \mu\text{l/h} < Q < 15 \mu\text{l/h}$. For $d = 11 \mu\text{m}$, the fraction of undamaged aggregates (green) is maximal in classes 3 and 4, up to 67%, exceeding the fraction in class 1 by more than five times. If the aggregate size continues to increase, the probability of undamaged aggregates decreases. The proportion of damaged aggregates (yellow), on the other hand, increases with aggregate size from 5% to up to 74%. At a stenosis width of $11 \mu\text{m}$, it can be clearly seen that the narrowing of the cross-section is not sufficient to affect the large aggregates. Only 3% of the largest aggregates are totally disrupted.

Overall, the same trends that occur for rosettes can be found here. The narrower and the longer the stenosis, the more aggregates are damaged or disintegrated. Having a closer look at the survival quantities in Figure 3 for rosettes and Figure 5 for lectin-induced aggregates, as summarized in Table 1, lectin-induced aggregates appear to be less stable than rosettes. Looking at the average survival for all size classes, for $d = 7 \mu\text{m}$, for example, only about 30% of rosettes are totally disrupted, but about 60% of lectin-induced aggregates are. The situation is even more pronounced for $d = 5 \mu\text{m}$. Here, only 10–20% of the lectin-induced aggregates remain undamaged, while approx. 70-90% are totally disrupted. For rosettes, the same conditions result in 20–30% undamaged and only about 70% totally disrupted.

Survival rate					Undamaged rate				
5 μm	0.2 EL	EL	2 EL	3 EL	5 μm	0.2 EL	EL	2 EL	3 EL
BG O	81%	45%	36%	35%	BG O	62%	29%	15%	14%
BG A	90%	50%	30%	23%	BG A	69%	34%	17%	11%
Lectin	41%	27%	9%	8%	Lectin	6%	16%	6%	5%

Survival rate					Undamaged rate				
7 μm	0.2 EL	EL	2 EL	3 EL	7 μm	0.2 EL	EL	2 EL	3 EL
BG O	81%	75%	79%	56%	BG O	61%	46%	42%	29%
BG A	90%	91%	87%	74%	BG A	69%	58%	48%	41%
Lectin		30%	25%	38%	Lectin		23%	15%	23%

Table 1 Survival and undamaged rates independent of the cell aggregate size (weighted average over all classes) for blood groups A and O (compare Figure 3) and Lectin-induced aggregates (compare Figure 5).

To further compare the stability of rosettes and Lectin-induced aggregates, we repeat the analysis from Figure 4 and evaluate the survival rate s as a function of elongation length for the Lectin-induced aggregates (Figure 6). As already observed for rosettes, the curves for the narrower stenosis with $d = 5 \mu\text{m}$ drop systematically, whereas the level at $d = 7 \mu\text{m}$ does not seem to depend significantly on the elongation length. For the experimentally obtained survival rate of rosettes, equation 1 allowed us to determine the transition length e^* at a survival rate of 50%. Here, in Figure 6A, the values barely exceed the 50% mark. Thus, the fitted transition lengths are very short with $e^* < 10 \mu\text{m}$ compared to the transition lengths $e^* = 50\text{--}100 \mu\text{m}$ we found for rosettes, compare Figure 4.

Rosettes and lectin-induced aggregates thus behave qualitatively similarly. Cell-cell binding, which is a specific ligand-receptor binding in both cases, seems to be significantly more stable for *PfEMP1*. Thus, lectin-induced aggregates are suitable as a qualitative model that captures the general trends of aggregate break-up in stenoses. However, since lectin-induced bonds are weaker and fewer than bonds in malaria aggregates, the quantitative behaviors are different.

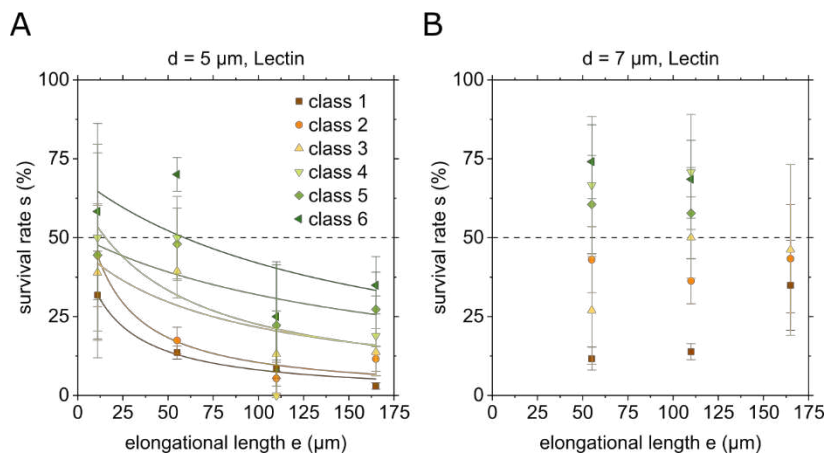


Figure 6 Elongation-induced disassembly of Lectin-induced aggregates. Survival rate s for aggregates of classes 1–6 as a function of elongation length upon passage of single stenoses of four different lengths from $e = 0.2 e_{Std} = 11 \mu\text{m}$ to $e = 3e_{Std} = 165 \mu\text{m}$ at fixed width A) $d = 5 \mu\text{m}$ and B) $d = 7 \mu\text{m}$. The error bars represent the 95% confidence intervals. A) Resulting transition lengths e^* : $e^*(\text{class 1}) = 0.1 \mu\text{m}$, $e^*(\text{class 2}) = 8 \mu\text{m}$, $e^*(\text{class 3}) = -4 \mu\text{m}$, $e^*(\text{class 4}) = 15 \mu\text{m}$, $e^*(\text{class 5}) = 3 \mu\text{m}$, $e^*(\text{class 6}) = 59 \mu\text{m}$.

For both rosettes and other cell aggregates, the shape of the stenosis strongly determines the ability of the cell aggregate to pass through it. Firstly, the diameter d is relevant. If d is narrow

enough to impair the rosettes or aggregates noticeably, the length e of the narrowing part plays an important role. An abrupt constriction is less fatal than the continuous narrowing over a longer distance. During passing such a constriction a rosette can be deformed by compressing the entire rosette and the rearrangement of the cells. How much cells are moved relatively to each other, and whether the bonds can persist during the process, is most likely dependent on the exposure time inside the stenosis and therefore its length. To further elucidate the role of the elongation length, we designed a simple simulation of the protein binding kinetics.

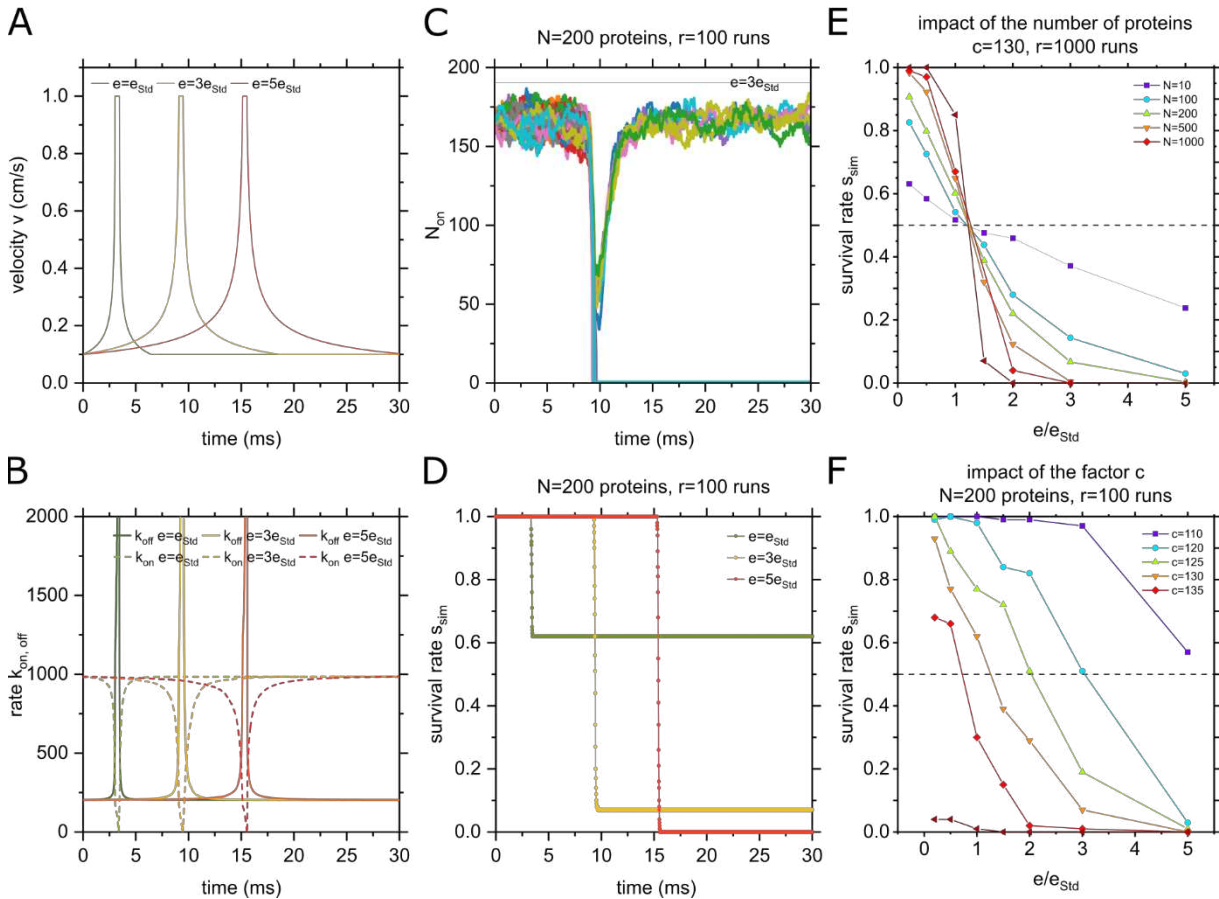


Figure 7 Simulation of the protein binding kinetics. A) velocity and B) tie-on and tie-off rates for three different elongational lengths with number of proteins $N_{total} = 200$ and $c = 130$. C) Simulation result $N_{on}(t)$ for $N_{total} = 200$, $e = 3e_{Std}$ and 100 runs and D) survival rate as a function of time for $e = e_{Std}$, $e = 3e_{Std}$ and $e = 5e_{Std}$. E) Simulated survival rate as a function of elongational length for different numbers of proteins N_{total} from $r=1000$ runs per value of N_{total} , and $r=100$ runs for $N_{total} = 1000$. F) Simulated survival rate as a function of elongation length for $N_{total} = 200$ proteins for different values of c .

Survival rate for different elongation lengths – Simulation of the protein binding kinetics

Using a Monte Carlo approach, the states of a certain number of proteins ($N = 10$ to $N = 1000$) were simulated under the influence of a force equivalent to the passage of a stenosis. The velocity (Figure 7A) significantly determines the tie-off and tie-on rates $k_{on,0}$ and $k_{off,0}$, compare Figure 7B. An example of $r = 100$ runs with $N = 200$ proteins is shown in Figure 7C. We see the number of proteins in the bound state N_{on} as a function of time. From these simulations, similar to the analysis of the experiments, a survival rate s_{sim} is determined (compare Figure 7D and equation 9). We compare the survival rate s_{sim} from simulating the protein binding kinetics with the experimental survival rate s_{exp} from Figure 4.

First, results of different variants of the simulation are presented. With the parameters $v_0 = 0.01$ m/s, $\Delta t = 10$ μ s, $k_{on,0} = 1000$ and $k_{off,0} = 200$, the survival rate is obtained as a function of the elongation length as shown in Figure 7E and F. The progression is strongly related to the number of proteins chosen for the simulation and the factor c used to calculate the rate according to equation 9. According to the estimation in equation 8, $c = 130$ was used. The transition length, at which a survival rate of 50% is achieved, shifts to smaller values with increasing factor c , see Figure 7F. For different protein numbers, the transition length is constant, but the curve becomes significantly steeper with increasing number of simulated proteins, see Figure 7E. After comparison with Figure 4A, the curve for $c = 130$ and $N_{total} = 200$ proteins and binding sites, respectively, corresponds most closely to the experimental results of rosettes. In addition, the value of the transition length with $e \approx 1.25e_{Std} = 69\mu\text{m}$ is in the range of the transition lengths of 50–100 μm determined in the experiment, see Figure 4B.

The reduction of the absolute values of $k_{on,0}$ and $k_{off,0}$ at the same ratio essentially preserves position and shape of the step in $s(e)$. While reducing the tie-on and tie-off rates for constant $k_{on,0}/k_{off,0}$ results in the same equilibrium number of bound proteins, the dynamics are different. Here, especially the return to equilibrium after passing the stenosis runs slower with lower absolute values of $k_{on,0}$ and $k_{off,0}$. In order to keep the process out of a deterministic regime, $P = k\Delta t$ must remain significantly smaller than 1. A capping of the rate with $P_{max} = 0.5$ has no influence on the results, even with $P_{max} = 0.1$ the difference is small or leads to higher survival rates only for short elongation lengths. Shortening of the time steps to one tenth resulted in identical curves (results not shown here).

Based on the experimentally determined results presented in Figure 3 and 4 we adjusted the original hypothesis as follows. We assume that the increased exposure time (in the range of 5–10 ms) that comes with an increased elongation length contributes stronger to rosette disruption than the decreased elongation rate reduces the probability for rosette disruption. Summarizing the Monte Carlo simulations, we obtained the same qualitative and quantitative trends for the survival rate as in the experiments. The best agreement was obtained for $N_{total} = 200$. Thus, these simulation results are in line with our adapted hypothesis.

However, the Monte Carlo model is limited to the level of individual proteins, and the shape of the red blood cells is disregarded. In order to simulate aggregates of deformable red blood cells passing the stenosis, as an outlook we additionally use an established lattice-Boltzmann-finite-element method (21).

Lattice-Boltzmann-finite-element simulations

There is a scarcity of simulations of RBC aggregates flowing in complex geometries. Previous simulations include aggregates in simple shear flow in two dimensions (25–28) or pairs of RBCs passing through constrictions in three dimensions (29–31) or multiple aggregated RBCs facing a bifurcation (32). In the present work, we simulated aggregates of three and five cells mimicking the experiments.

Healthy RBCs were assumed to have a shear elasticity of 5 $\mu\text{N}/\text{m}$ while the infected cells were modeled with a tenfold value to resemble the membrane stiffening during infection. These numbers are simplified based on experimental data showing a shear elasticity of 8 $\mu\text{N}/\text{m}$ for healthy RBCs and a 2–7-fold increase depending on the time *post invasion* (33). For all simulations we used a voxel size of 0.5 μm and RBC meshes with 1280 triangular elements.

The first step was to find suitable parameters for the Morse potential, equation 10, which models the RBC aggregation. For numerical efficiency reasons, we set $r_0 = 0.5$ μm and $\beta =$

$4\mu\text{m}^{-1}$. In order to obtain the value for the interaction strength S , we considered a pair of an infected and an unparasitized RBC in simple shear flow. Experiments have shown that cells detach from rosettes at shear stresses in the range of 0.5–2.5 Pa (34) and 1.0–1.6 Pa (7, 35), respectively. We adjusted the parameter S such that both cells detached from each other within 0.04 s under a shear stress of 1.2 Pa.

Once the parameters of the Morse potential had been established, we simulated aggregates of three and five cells. Each aggregate comprised of a central infected RBC and several

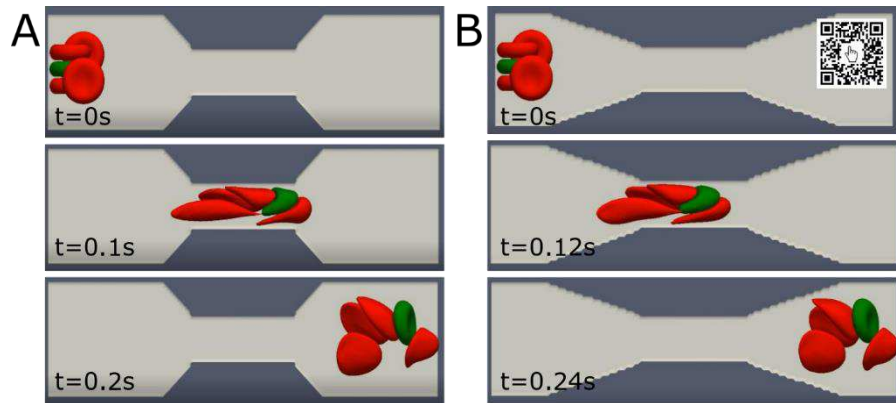


Figure 8 Five-cell aggregate during passage of a stenosis with standard length $l = 20 \mu\text{m}$ and (A) steep angle of 50° or (B) one with a flat 19° angle. The behavior observed in A) and B) is almost identical.

surrounding uninfected RBCs. The simulated geometries had an overall length of $75 \mu\text{m}$, an unconstricted width of $21 \mu\text{m}$, and a constant depth of $17 \mu\text{m}$. Figure 8 shows example snapshots of a five-cell aggregate flowing through two types of constrictions mimicking the experimental geometry.

Based on the standard stenosis shape of stenosis width $d = 8 \mu\text{m}$, constriction angle $\alpha = 31^\circ$ and $l = 20 \mu\text{m}$ length, we chose the following versions listed in Table 2. The selection includes two variations of elongation length and thus constriction angle of $\alpha = 19^\circ$ (see Figure 8A), and $\alpha = 50^\circ$ (see Figure 8 B), two variations of the stenosis width $d = 4 \mu\text{m}$ and $d=11 \mu\text{m}$, and two variations of the length of the narrowest part of $l = 5 \mu\text{m}$ and $l=40 \mu\text{m}$.

Stenosis	Stenosis width d	Stenosis angle α	Stenosis length l	Survival rate	
				Three-cell aggregate	Five-cell aggregate
Standard	$8 \mu\text{m}$	31°	$20 \mu\text{m}$	100%	0%
Version $\alpha 1$	$8 \mu\text{m}$	19°	$20 \mu\text{m}$	60%	0%
Version $\alpha 2$	$8 \mu\text{m}$	50°	$20 \mu\text{m}$	100%	0%
Version $d 1$	$4 \mu\text{m}$	31°	$20 \mu\text{m}$	100%	0%
Version $d 2$	$11 \mu\text{m}$	31°	$20 \mu\text{m}$	100%	0%
Version $l 1$	$8 \mu\text{m}$	31°	$5 \mu\text{m}$	100%	0%
Version $l 2$	$8 \mu\text{m}$	31°	$40 \mu\text{m}$	60%	0%

Table 2 Simulated stenosis geometries and observed survival rates.

The simulations showed that, for three-cell aggregates, cell loss occurred in the longest stenosis in two out of five simulated passages. In the shorter stenoses, however, no cell loss was observed. This result highlights that longer stenoses and less steep constriction angles are more difficult for aggregates to pass, which is in line with the experimental findings.

The five-cell aggregates suffered from cell loss in all simulated cases. We found that usually two cells were sheared off the aggregate in the constriction. This cell loss was caused by a reduced contact area between the surrounding unparasitized cells and the infected cell during the passage.

The simulations qualitatively confirm the trends observed in the experiments. For a quantitative comparison, a separate extensive study with a large number of simulations would be necessary. Such a thorough investigation could reveal detailed cell dynamics leading to aggregate damage and its interplay with the stenosis geometry and flow field.

CONCLUSION

In this study, the stability of malaria infected red blood cell aggregates, so called rosettes, during passage of stenoses with different elongation lengths and thus different times of exposure to elongation forces acting on the cell aggregates was investigated. Rosettes were tracked along the channel and categorized into the three states “undamaged”, “damaged” and “totally disrupted” after passage of a stenosis. We define the survival rate as the sum of the undamaged and damaged proportions. The focus was to elucidate the influence of the rosette size, blood group and geometry of the stenosis on the survival rate. Classification by size allowed us to highlight the differences in binding strength between blood groups O and A.

The key findings are that larger rosettes, which can afford losing more cells before being considered disrupted, tend to be more durable. Second, a longer stenosis leads to more frequent disruption of the rosettes, implying that not higher elongational rates but longer exposure to elevated shear and elongational flow is critical. Model systems in experiment and simulation support these observations. To differentiate the impacts of elongational rate, exposure time and stenosis length in the future, a respective set of microchannels could be designed to vary each parameter individually.

Our findings are important as they identify mechanisms leading to aggregate disruption, which expose malaria-infected cells. Exposed malaria-infected cells are more accessible and easier to be cleared by the immune system. It would be fascinating to investigate the disruption dynamics of rosettes *in vivo*.

DECLARATION OF INTERESTS.

The authors declare no competing interests.

AUTHOR CONTRIBUTIONS.

A.M.J., M.W., T.K. and C.W. designed research. A.M.J., A.S., A.M., K.M., T.K. and C.W. performed research, A.M.J contributed analytic tools, A.M.J., A.S., A.M., K.M., T.K. and C.W analyzed data, A.M.J., T.K. and C.W. wrote the manuscript.

ACKNOWLEDGEMENT

A.M.J. and C.W. would like to acknowledge funding by Nanosystems Initiative Munich (NIM), the Center for NanoScience (CeNS), the “Studienstiftung des deutschen Volkes,” and the “Programm für Chancengleichheit” of the University of Augsburg for financial support, allowing for, among others, several research stays at the Karolinska Institute. Moreover, we thank Gerhard Schmid for fruitful discussions.

LITERATURE

1. Moll, K., M. Palmkvist, J. Ch'ng, M.S. Kiwuwa, and M. Wahlgren. 2015. Evasion of Immunity to Plasmodium falciparum: Rosettes of Blood Group A Impair Recognition of PfEMP1. *PLoS One*. 10: e0145120.
2. Paing, M.M., N.D. Salinas, Y. Adams, A. Oksman, A.T.R. Jensen, D.E. Goldberg, and N.H. Tolia. 2018. Shed EBA-175 mediates red blood cell clustering that enhances malaria parasite growth and enables immune evasion. *Elife*. 7: 1–18.
3. Vahidi, B., and N. Fatourae. 2012. Large deforming buoyant embolus passing through a stenotic common carotid artery: A computational simulation. *J. Biomech*. 45: 1312–1322.
4. Musoke, C., C. Ssendikadiwa, C. Babua, and J. Schwartz. 2014. Severe falciparum malaria associated with massive pulmonary embolism. *Ann. Afr. Med*. 13: 47–49.
5. Okeniyi, J., and B. Kuti. 2008. Cerebral Malaria in Children with Cyanotic Heart Diseases - The Need for a Closer Look. .
6. McQuaid, F., and J.A. Rowe. 2020. Rosetting revisited: A critical look at the evidence for host erythrocyte receptors in Plasmodium falciparum rosetting. *Parasitology*. 147: 1–11.
7. Nash, G.B., B.M. Cooke, J. Carlson, and M. Wahlgren. 1992. Rheological properties of rosettes formed by red blood cells parasitized by Plasmodium falciparum. *Br. J. Haematol*. 82: 757–63.
8. Chu, Y., T. Haigh, and G. Nash. 1997. Rheological analysis of the formation of rosettes by red blood cells parasitized by Plasmodium falciparum. *Br. J. Haematol.* : 777–783.
9. Adams, Y., and J.A. Rowe. 2013. The effect of anti-rosetting agents against malaria parasites under physiological flow conditions. *PLoS One*. 8: e73999.
10. Jötten, A.M., K. Moll, M. Wahlgren, A. Wixforth, and C. Westerhausen. 2020. Blood group and size dependent stability of P. falciparum infected red blood cell aggregates in capillaries. *Biomicrofluidics*. 14: 024104.
11. Sing, C.E., and A. Alexander-Katz. 2010. Elongational Flow Induces the Unfolding of von Willebrand Factor at Physiological Flow Rates. *Biophys. J*. 98: L35–L37.
12. Moll, K., I. Ljungström, H. Perlmann, A. Scherf, and M. Wahlgren. 2008. Methods in Malaria Research. Evaluation. : 1-3,17-21.
13. Xia, Y., and G.M. Whitesides. 1998. Soft Lithography. *Annu. Rev. Mater. Sci*. 28: 153–184.
14. Jötten, A.M. 2021. SURF Survival of Rosettes in Flow. .
15. Zhu, C. 2000. Kinetics and mechanics of cell adhesion. *J. Biomech*. 33: 23–33.
16. Rakshit, S., and S. Sivasankar. 2014. Biomechanics of cell adhesion: How force regulates the lifetime of adhesive bonds at the single molecule level. *Phys. Chem. Chem. Phys*. 16: 2211–2223.
17. Bell, G.I. 1978. Models for the specific adhesion of cells to cells. *Science (80-.)*. 200: 618–627.
18. Scherer, P.O.J., and S.F. Fischer. 2017. Kramers Theory. In: *Theoretical Molecular*

Biophysics. Berlin, Heidelberg: Springer Berlin Heidelberg. pp. 113–118.

19. Quadt, K.A., L. Barfod, D. Andersen, J. Bruun, B. Gyan, T. Hassenkam, M.F. Ofori, and L. Hviid. 2012. The Density of Knobs on Plasmodium falciparum-Infected Erythrocytes Depends on Developmental Age and Varies among Isolates. *PLoS One*. 7: 1–8.
20. Qian, Y.H., D. D’Humières, and P. Lallemand. 1992. Lattice bgk models for navier-stokes equation. *Epl*. 17: 479–484.
21. Krüger, T., M. Gross, D. Raabe, and F. Varnik. 2013. Crossover from tumbling to tank-treading-like motion in dense simulated suspensions of red blood cells. *Soft Matter*. 9: 9008–9015.
22. Peskin, C.S. 2002. The immersed boundary method. *Acta Numer*. 11: 479–517.
23. Ladd, A.J. 1994. Numerical simulations of particulate suspensions via a discretized Boltzmann equation. Part 1. Theoretical foundation. *J. Fluid Mech*. 271: 285–309.
24. Carlson, J. 1992. Plasmodium falciparum erythrocyte rosetting is mediated by promiscuous lectin-like interactions. *J. Exp. Med*. 176: 1311–1317.
25. Mountrakis, L., E. Lorenz, and A.G. Hoekstra. 2016. Scaling of shear-induced diffusion and clustering in a blood-like suspension. *Epl*. 114: 1–6.
26. Wang, T., Z. Xing, and D. Xing. 2013. Structure-induced dynamics of erythrocyte aggregates by microscale simulation. *J. Appl. Math*. 2013.
27. Xu, D., E. Kaliviotis, A. Munjiza, E. Avital, C. Ji, and J. Williams. 2013. Large scale simulation of red blood cell aggregation in shear flows. *J. Biomech*. 46: 1810–1817.
28. Wang, T., Y. Tao, U. Rongin, and Z. Xing. 2016. A Two-Dimensional Numerical Investigation of Transport of Malaria-Infected Red Blood Cells in Stenotic Microchannels. *Biomed Res. Int*. 2016.
29. Li, H., T. Ye, and K.Y. Lam. 2014. Computational Analysis of Dynamic Interaction of Two Red Blood Cells in a Capillary. *Cell Biochem. Biophys*. 69: 673–680.
30. Ye, T., N. Phan-Thien, B.C. Khoo, and C.T. Lim. 2014. Dissipative particle dynamics simulations of deformation and aggregation of healthy and diseased red blood cells in a tube flow. *Phys. Fluids*. 26.
31. Xiao, L., Y. Liu, S. Chen, and B. Fu. 2016. Simulation of Deformation and Aggregation of Two Red Blood Cells in a Stenosed Microvessel by Dissipative Particle Dynamics. *Cell Biochem. Biophys*. 74: 513–525.
32. Ye, T., and L. Peng. 2019. Motion, deformation, and aggregation of multiple red blood cells in three-dimensional microvessel bifurcations. *Phys. Fluids*. 31.
33. Ademiloye, A.S., L.W. Zhang, and K.M. Liew. 2017. A three-dimensional quasicontinuum approach for predicting biomechanical properties of malaria-infected red blood cell membrane. *Appl. Math. Model*. 49: 35–47.
34. Chotivanich, K.T., A.M. Dondorp, N.J. White, K. Peters, J. Vreeken, P.A. Kager, and R. Udomsangpetch. 2000. The resistance to physiological shear stresses of the erythrocytic rosettes formed by cells infected with Plasmodium falciparum. *Ann. Trop. Med. Parasitol*. 94: 219–226.
35. Lee, W.-C., B. Russell, and L. Rénia. 2019. Sticking for a Cause: The Falciparum Malaria

Parasites Cytoadherence Paradigm. *Front. Immunol.* 10.